CrossMark

TECHNICAL PAPER

MHD natural convection phase-change heat transfer in a cavity: analysis of the magnetic field effect

Ali Doostani[1] · Mohammad Ghalambaz[1] · Ali J. Chamkha[2,3]

Abstract The present study aims to investigate the effect of the presence of a uniform magnetic field on the rate of melting and melting behavior of an electrically-conducting material in an enclosure. The left and right walls of the cavity are isothermal at hot and cold temperatures, respectively. The top and bottom walls are adiabatic. The phase-change process is formatted using the enthalpy-porosity model by considering a fixed computational grid. The governing equations are transformed into a non-dimensional form and then solved by the aid of the finite element method. The results of the present study are compared with the experimental and numerical data available in the literature and are found to be in good agreement. In order to investigate the effect of magnetic field on the melting process, the results of the present study are reported for various values of the Hartmann number in the range 0–100. The results show that increasing of the Hartmann number reduces the melting volume fraction and tends to suspend the convective mechanisms. However, high magnetic fields induce more uniform temperature gradients. Therefore, using a strong magnetic field can have a significant impact on the melting control process of electrically-conducting materials.

Keywords Phase-change materials · Magnetic field · Natural convection · Cavity

List of symbols

A_{mush}	Mushy-zone constant (Carman–Koseny equation constant)
B_0	Magnetic induction
C	Specific heat (J/kg K)
c_1–c_4	Coefficients of the basis
C_p	Specific heat in constant pressure (J/kg K)
g	Gravity (m/s^2)
Ha	Hartmann number
k	Thermal conductivity (W/m K)
L	Latent heat of fusion (J/kg)
L_x	Length x-direction (m)
L_y	Length y-direction (m)
$\overline{Nu}$	Average Nusselt number
P	Pressure (Pa)
Pr	Prandtl number
Ra	Rayleigh number
Re	Reynolds number
S	Enclosure inclination angle
$S(T)$	Carman–Koseny equation (source term)
Ste	Stefan number
T	Temperature (K)
t	Time (s)
T_f	Melting temperature (K)
u	Velocity in the x-direction (m/s)
v	Velocity in the y-direction (m/s)

✉ Mohammad Ghalambaz
m.ghalambaz@iaud.ac.ir

Ali Doostani
doostaniali@gmail.com

Ali J. Chamkha
achamkha@pmu.edu.sa

[1] Department of Mechanical Engineering, Dezful Branch, Islamic Azad University, Dezful, Iran

[2] Mechanical Engineering Department, Prince Mohammad Bin Fahd University, Al-Khobar 31952, Kingdom of Saudi Arabia

[3] Prince Sultan Endowment for Energy and Environment, Prince Mohammad Bin Fahd University, Al-Khobar 31952, Kingdom of Saudi Arabia

⚛ Springer

Greek symbols

α	Thermal diffusivity (m^2/s)
ΔT	Mushy-zone temperature range (K)
μ	Dynamic viscosity (kg/m s)
μ_0	The permeability of free space
ε	Carman–Koseny equation constant
θ	Non-dimensional temperature
ξ	Basis functions
$\varphi(T)$	Liquid fraction
β	Thermal expansion coefficient (1/K)
γ	The ratio of thermal diffusivity
ρ	Density (kg/m^3)
σ	Electrical conductivity
ν	Kinematic viscosity (m^2/s)

Subscripts

c	Cold
F	Fusion
h	Hot
i	Interface position
k	Node number
l	Liquid phase
m	Magnetic field
s	Solid phase

1 Introduction

The natural convection heat transfer in an enclosure with isothermal side walls has been investigated in many previous studies. The natural convection in a cavity is important due to its applications in cooling of electronic packages, solar technology, crystal growth in liquids, glass melting, isolation in buildings, and safety aspects of gas cooled reactors. In many of these applications, the performance of the system and the quality of the final product are influenced by the temperature distribution and heat transfer rates in the system. For example, in a casting process, the fragmentation of crystals is a direct function of the temperature treatment [1]. The presence of a magnetic field could result in formation of textures along an easy-magnetization axis in a casting process of a metallic melt for producing of a textured material [2].

In a cavity filled with a fluid, the presence of the temperature difference induces a buoyancy force which results in fluid motion. This phenomenon is known as "natural convection". When the cavity is filled with an electrically conducting liquid and subject to a magnetic field, the moving fluid experiences the Lorentz force and its effect is to resist the fluid motion [3]. This effect, consequently, alters the heat transfer rate and the temperature distribution in the cavity. Thus, the magnetic field in magnetohydrodynamic flows (MHD) may be utilized as a controlling agent for the flow and temperature distributions in the cavity in order to increase the quality of some products. For instance, the action at a distance of a magnetic field on the metals processing industry include the control of liquid metals in continuous casting process and electro-magnetically supported melts [4]. Another important application of liquid metals is in nuclear engineering applications. The metal coolants are much denser than the conventional liquids such as water which has been utilized in power plants. The metal liquids can remove heat more rapidly, and hence, they can provide much higher power density compared to water. Moreover, the cooling with water requires a high pressurized system to raise the boiling point of the water. The higher the pressure is, the higher the safety maintenance issues are. In contrast, the liquid metals can be utilized at very high temperatures in a low pressurized system. Another important advantage of liquid metals is its radiation shielding properties that makes them attractive in nuclear applications. As the liquid metals are highly electrically conducting, they can be pumped using an electromagnetic field [5].

In recent years, the effect of magnetic field has been examined on the convective heat transfer of MHD flows in molten electrically-conducting liquids. Sathiyamoorthy and Chamkha [6, 7] have studied the effect of a magnetic field on the natural convection heat transfer of molten gallium for various magnetic field inclination angles and uniformly or linearly heated adjacent walls. Gontijo and Cunha [8] have experimentally investigated the heat transfer rate and the thermo-magnetic convection inside a cavity with an aspect ratio near unity. They reported that by using a very dilute suspension of a magnetic composite with a particle volume fraction of 0.5%, the average temperature of the fluid inside a cavity decreases up to 10% and the Nusselt number increases about 10% by applying a moderate magnetic field. Maatki et al. [9] have investigated the convection heat transfer of a binary mixture in a three-dimensional cavity in the presence of a magnetic field.

Selimefendigil et al. [10] have analyzed the effect of magnetic field on the natural convection of ferrofluids in a differentially-heated cavity in which the hot wall is subjected to partial heating while the rest of the wall is insulated. The authors have examined the effect of a magnetic dipole on the natural convective heat transfer in the cavity. Sheikholeslami et al. [11] have considered the enclosure space between two tubes where the inner tube is elliptic shape. The authors have studied the MHD natural convection heat transfer of CuO nanofluids in the enclosure. They found an increase of heat transfer enhancement by the increase of the magnetic field. Jena et al. [12] have studied the effect of the magnetic field on the natural convective heat transfer of molten gallium in a three-dimensional cavity heated from below. Malvandi et al. [13] have studied the effect of magnetic field on the convection heat transfer of

a magnetic nanofluid inside a vertical channel. They concluded that the presence of a magnetic field reduces the thermal advantages of nanofluids. Adesanya et al. [14] have analyzed the free convective flow of an MHD fluid through a channel with time periodic boundary condition by considering the effects of Joule dissipation. Chamkha et al. [15] have investigated the entropy generation in a differentially-heated cavity filled with a CuO-water nanofluid by considering the effect of a magnetic field. The authors reported that the magnetic field can suppress the entropy generation rate.

Mojumder et al. [16] have studied the effect of magnetic field on the natural convection and entropy generation of a magnetic nanofluid in a half-moon shaped cavity with semi-circular bottom heater considering various values of the magnetic parameter and different inclination angles of cavity and the position effect of the heaters. Selimefendigil et al. [17] have addressed the effect of magnetic field strength and angle on the convective heat transfer of CuO nanofluids in a lid-driven cavity. They found that the angle of the magnetic field shows a significant effect of on the convective heat transfer rate and that the presence of a magnetic field reduces the convective heat transfer in the cavity. Rashidi et al. [18] have investigated the effect of a magnetic field on the mixed heat transfer in a channel with a sinusoidal wall filled with Al_2O_3 nanofluid. They reported an enhancement of heat transfer in the presence of the magnetic field. In all of the mentioned studies, the effect of the presence of a magnetic field on the flow and heat transfer in a cavity has been studied for fluids in liquid phase without any phase change.

There are some experimental and numerical studies regarding solid–liquid phase-change involving natural convection effects. Gau and Viskanta [19] have performed experimental test for measuring the melting interface of solidification of a pure metal (Gallium). Following the study of Gau and Viskanta [19], Brent et al. [20] have reported a numerical solution for melting of Gallium in a rectangular differentially-heated cavity using a fixed grid approach known as the enthalpy-porosity technique. They compared the obtained numerical results with the experimental results of Gau and Viskanta [19] and found comparatively a good agreement. Bertrand et al. [21] have performed a benchmark numerical study for melting simulation of solid in a rectangular cavity by considering the natural convection effects. Various numerical methods in different laboratories were utilized to simulate the melting process of Tin and Octadecane.

Fan and Khodadadi [22] have reported an excellent review of the heat transfer studies regarding to simulation and experiments of phase-change material. Very recently, Kumar et al. [23] have experimentally analyzed melting of a cuboid lead subject to a constant heat flux boundary

condition. A neutron radiography method was employed to visualize the melting interface. Then, an image processing technique was utilized to extract the molten interface radiography images. It is worth noticing that the lead provides shielding effects and is important in the design of transportation packages for nuclear material. Kumar et al. [24] have also experimentally studied the effect of boundary heat flux conditions on the melting behavior of a cuboid lead using an infra-red thermography technique. The results indicate that the buoyancy effects are very important in the melting of lead for Rayleigh number of order 10^7.

Ranjbar et al. [25] and Kashani et al. [26] have studied solidification of a nano-enhanced phase-change material (NEPCM) in a wavy cavity. Tiari et al. [27] have examined the effect of the presence of a fin (heat-pipe type) on the phase-change behavior of a high melting temperature phase-change material. Tiari et al. [28] have also studied the melting behavior of potassium nitrate as phase-change material in a cavity supported with heat-pipe type fins.

The present study aims to theoretically address the influence of a uniform magnetic field on the phase-change behavior of an electrically-conducting material involving natural convection effects.

2 Geometric and mathematical models

2.1 Formulation of the problem

Consider a cavity with the width L_x and height L_y. A schematic view of the physical model is represented in Fig. 1. This figure shows a two-dimensional square cavity filled with an electrically-conducting frozen substance such as gallium or an electrolyte with a fusion temperature T_f. The right and left walls of the cavity are at the isothermal temperatures T_c and T_h where $T_h > T_f > T_c$. The bottom and top walls are insulated. As depicted in Fig. 1, in the melting process, three states in the cavity can be assumed, a fully solid state, the mushy state and the fully liquid state. The mushy region state is a two-phase region that is a mixture of the solid and liquid phases. In the mushy region, the volume fractions of the liquid and the solid are functions of the temperature which will be discussed in details later. It is assumed that the cavity is initially filled with a solid substance at the fusion temperature T_f. A uniform magnetic field with magnitude B_0 is applied normal to the vertical walls as shown in Fig. 1.

2.2 Governing equations

All of the enclosure walls are considered to be impermeable and the no-slip velocity boundary conditions is employed. The top and bottom walls are considered well insulated and

Fig. 1 Schematic diagram of physical model
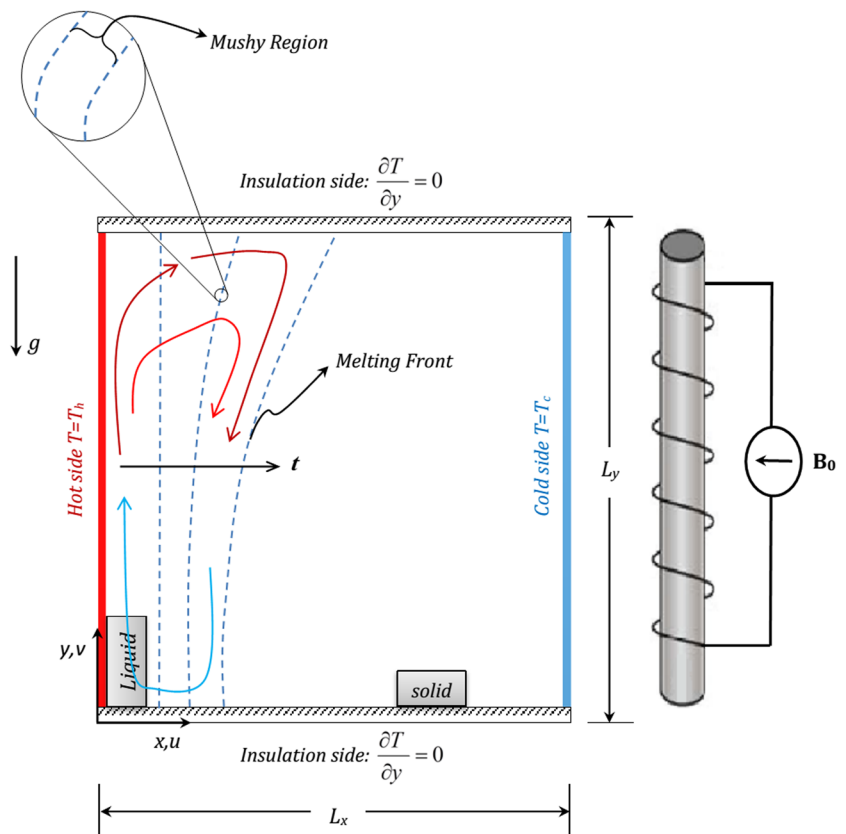
the side walls are isothermal. All of the enclosure walls are assumed perfectly electrically-conducting. Moreover, the Boussinesq approximation is adopted. The temperature differences are assumed to be small, and hence, the thermophysical properties in each phase are assumed to be constant, and the Boussinesq approximation is applicable for considering the density changes in liquid phase. However, the thermo-physical changes due to phase change are taken into account as the density, heat capacity and thermal conductivity for the solid and liquid phases of a substance could be different. It is also assumed that Joule heating effects as well as the viscous dissipation effects and radiation effects are negligible. The induced magnetic field due to the induced current in the cavity is neglected as the magnetic Reynolds number (Re_m) is small Indeed, the magnetic Reynolds number ($Re_m = uL/(\mu_0\sigma)$) shows the ratio of the induction of a magnetic field by the motion of the fluid to the magnetic diffusion where u is the velocity scale, L is the flow length scale, μ_0 is the permeability of free space, and σ is the electrical conductivity of the liquid. Here, it is assumed that the induced magnetic field, produced by the motion of the electrically-conducting fluid, is negligible compared to the applied magnetic field B_0. Considering the above assumptions, the conservation equations for mass, momentum, temperature and electric transfer are written as:

Continuity

$$\nabla \cdot \mathbf{u} = 0 \tag{1}$$

Momentum

$$\frac{\partial \mathbf{u}}{\partial t} + (\mathbf{u} \cdot \nabla)\mathbf{u} = -\frac{1}{\rho}\nabla P + \nu\nabla^2\mathbf{u} + \frac{\mathbf{J}}{\rho} \times \mathbf{B} + \beta\mathbf{g}(T - T_f) + S(T)\mathbf{u} \tag{2}$$

Energy

$$\frac{\partial T}{\partial t} + (\mathbf{u}).\nabla T = \alpha\nabla^2 T - \frac{L}{C_p}\frac{\partial\varphi(T)}{\partial t} \tag{3}$$

Electric transfer

$$\mathbf{J} = \sigma(-\nabla\phi + \mathbf{u} \times \mathbf{B}) \tag{4a}$$

$$\nabla^2\phi = \mathbf{B} \cdot \omega, \quad \omega = \nabla \times \mathbf{u}, \tag{4b}$$

where $\mathbf{u}$, $\mathbf{B}$, ω, ϕ and $\mathbf{J}$ are the velocity, the magnetic field, the vorticity and the voltage field (the electric potential), and the current density, respectively. The variables P, T, and ϕ denote the pressure, the temperature, and the volume fraction of the liquid phase, respectively. Here, t is time and g is the vector of gravitational acceleration constant. In addition, α is the thermal diffusivity, L is the latent heat of fusion, C_p is the heat capacity at constant pressure, ρ is the density, β is the thermal expansion coefficient, ν is the kinematic viscosity, and σ is the electric conductivity. In

Eq. (2), the term $S(T) \cdot u$ indicates a source term for forcing the fluid velocity to zero in solid phase which will be discussed in more details later. The subscripts of s and l denote the solid and liquid phases, respectively.

Sreenivasan et al. [29] discussed the effect of magnetic field on the flow motion and concluded that for the case of 2D steady flow in the cases in which the magnetic field lies in the plane of the fluid motion and concluded that the term $B \cdot \omega$ is zero; hence, the governing equations of Eq. (4a, 4b) reduces to $\nabla^2 \phi = 0$. Taking into account that the enclosure walls are perfectly electrically-conducting, they could provide a very low resistance guide path for the induced current. Indeed, perfectly conducting walls provide a resistance-free path from the induced current which indicates that the electric field vanishes everywhere in the cavity, i.e. $\nabla \phi = 0$. Therefore, it can be concluded that the electric field can be neglected inside the enclosure [6].

Invoking these conditions, the team of $\mathbf{J} \times \mathbf{B}$ in the momentum equation reduces to $\sigma \mathbf{B}^2$ [7]. Thus, the governing equations for mass, momentum and thermal energy represented here in dimensional Cartesian coordinates x, y as follows:

Continuity

$$\frac{\partial u}{\partial x} + \frac{\partial v}{\partial y} = 0 \tag{5}$$

Momentum in x-direction

$$\rho \left(\frac{\partial u}{\partial t} + u \frac{\partial u}{\partial x} + v \frac{\partial u}{\partial y} \right) = -\frac{\partial p}{\partial x} + \mu \left(\frac{\partial^2 u}{\partial x^2} + \frac{\partial^2 u}{\partial y^2} \right) + S(T)\,u \tag{6}$$

Momentum in y-direction

$$\rho \left(\frac{\partial v}{\partial t} + u \frac{\partial v}{\partial x} + v \frac{\partial v}{\partial y} \right) = -\frac{\partial p}{\partial y}$$
$$+ \mu \left(\frac{\partial^2 v}{\partial x^2} + \frac{\partial^2 v}{\partial y^2} \right) + \rho g \beta (T - T_f) - (\sigma B_0^2)\,v + S(T)\,v \tag{7}$$

Energy

$$\frac{\partial T}{\partial t} + u \frac{\partial T}{\partial x} + v \frac{\partial T}{\partial y} = \alpha \left(\frac{\partial^2 T}{\partial x^2} + \frac{\partial^2 T}{\partial y^2} \right) + \frac{L}{c_p} \frac{\partial \varphi(T)}{\partial t}, \tag{8}$$

where $\alpha = \alpha_l \varphi + \alpha_s (1 - \varphi)$ and B_0 is the magnitude of the uniform magnetic field. Here, φ is the melt fraction which is evaluated using the temperature as:

$$\varphi(T) = \begin{cases} 0 & T < T_f \\ \frac{T - T_f}{\Delta T} & T_f < T < T_f + \frac{\Delta T}{2}, \\ 1 & T > T_f + \Delta T \end{cases} \tag{9}$$

where ΔT is the mushy-zone temperature range. The source term of $S(T)$ in the momentum equation is introduced as a continues equation for phase transient using the Carman–Koseny equation as [30, 31]:

$$S(T) = -A_{mesh} \frac{(1 - \varphi(T))^2}{\varphi(T)^3 + \varepsilon}, \tag{10}$$

where ε is a small number constant to prevent division by zero. In this study, the value of $\varepsilon = 10^{-3}$ is used as reported in similar studies in the open literature.

Based on the problem description, the boundary conditions are written as:

Heated wall $\quad x = 0, y = y : u = 0, v = 0, T = T_h \quad$ (K)

Cooled wall $\quad x = L_x, y = y : u = 0, v = 0, T = T_c \quad$ (11b)

Top wall $\quad x = x, y = L_y : u = 0, v = 0, \frac{\partial T}{\partial y} = 0 \quad$ (11c)

Bottom wall $\quad x = x, y = 0 : u = 0, v = 0, \frac{\partial T}{\partial y} = 0,$ (11d)

where L_x and L_y are the width and height of the enclosure, respectively. In addition, a reference pressure point with the relative pressure of zero is adopted at the top left corner of the enclosure. It is appropriate to express Eqs. (5)–(8) into the non-dimensional forms using dimensionless variables as following:

$$X = \frac{x}{L_y}, \quad Y = \frac{y}{L_y}, \quad U = \frac{u L_y}{\alpha_l}, \quad V = \frac{v L_y}{\alpha_l}, \quad \theta = \frac{T - T_f}{T_h - T_f} \tag{12a}$$

$$F_0 = \frac{t \alpha_l}{L_y^2}, \quad S(T) = \frac{S(T) L_y^2}{\rho \alpha_l}, \quad P = \frac{p L_y^2}{\rho \alpha_l^2},$$
$$\gamma = \frac{\alpha}{\alpha_l}, \quad R_k = \frac{k_s}{k_f}, \quad AR = \frac{L_y}{L_x} \tag{12b}$$

The relevant dimensionless parameters are then:

$$Ra = \frac{\rho^2 c_l g \beta L_y^3 (T_h - T_f)}{\mu k_l}, \quad Ste = \frac{c_l (T_h - T_f)}{L}, \quad Pr = \frac{c_l \mu}{k_l}, \quad Ha = B_0 L_y \sqrt{\frac{\sigma}{\rho \upsilon}}, \tag{13}$$

where Ra is the Rayleigh number, Ste is the Stefan number, Pr is the Prandtl number and Ha is the Hartmann number. Substituting Eqs. (12a, 12b) and (13) into Eqs. (5)–(8), the corresponding non-dimensional form of the governing Eqs. (14)–(17) is obtained as:

Continuity:

$$\frac{\partial U}{\partial X} + \frac{\partial V}{\partial Y} = 0 \tag{14}$$

Momentum in *x*-direction:

$$\frac{\partial U}{\partial F_0} + U\frac{\partial U}{\partial X} + V\frac{\partial U}{\partial Y} = -\frac{\partial p}{\partial X} + \text{Pr}\left(\frac{\partial^2 U}{\partial X^2} + \frac{\partial^2 U}{\partial Y^2}\right) + S(\theta)\,U \quad (15)$$

Momentum in *y*-direction:

$$\frac{\partial V}{\partial F_0} + U\frac{\partial V}{\partial X} + V\frac{\partial V}{\partial Y} = -\frac{\partial p}{\partial Y}$$
$$+ \text{Pr}\left(\frac{\partial^2 V}{\partial X^2} + \frac{\partial^2 V}{\partial Y^2}\right) + \text{Ra}\,\text{Pr}\,\theta - (\text{Ha})^2\,\text{Pr}\cdot V + S(\theta)\,V$$
$$(16)$$

Energy:

$$\frac{\partial \theta}{\partial F_0} + u\frac{\partial \theta}{\partial X} + v\frac{\partial \theta}{\partial Y} = \gamma\left(\frac{\partial^2 \theta}{\partial X^2} + \frac{\partial^2 \theta}{\partial Y^2}\right) - \frac{1}{\text{Ste}}\frac{\partial \varphi(\theta)}{\partial F_0}, \quad (17)$$

where

$$\gamma = \varphi(\theta) + \frac{\alpha_s}{\alpha_l}(1 - \varphi(\theta)) \quad (18)$$

In this way, in liquid zone ($\theta > 0$, $\varphi = 1$), $\gamma = 1$, and in the solid zone ($\theta < 0$, $\varphi = 0$), $\gamma = \frac{\alpha_s}{\alpha_l}$.

Upon using the variables introduced in Eq. (12a, 12b), the non-dimensional boundary conditions are:

Heated wall $X = 0 : U = 0, V = 0, \theta_h = 1$ (19a)

Cooled wall $X = 1 : U = 0, V = 0, \theta_c = \dfrac{T_c - T_f}{T_h - T_f}$ (19b)

Top wall $Y = \text{AR} : U = 0, V = 0, \dfrac{\partial \theta}{\partial Y} = 0$ (19c)

Bottom wall $Y = 0 : U = 0, V = 0, \dfrac{\partial \theta}{\partial Y} = 0,$ (19d)

where assuming the cold wall temperature T_c at the fusion temperature of T_f (i.e. $T_c = T_f$) gives $\theta_c = 0$.

The melt volume fraction as a function of θ is written as:

$$\varphi(\theta) = \begin{cases} 0 & \theta < 0 \\ \frac{\theta}{\Delta\theta} & 0 < \theta < \Delta\theta \\ 1 & \theta > \Delta\theta \end{cases}, \quad (20)$$

Table 1 The required time for grid size independency

Cases	Grid size	Run time
Case 1	100×100	14 h, 21 min
Case 2	125×125	1 day, 6 h, 12 min
Case 3	150×150	2 days, 1 h, 20 min
Case 4	175×175	2 days, 18 h, 27 min
Case 5	200×200	3 days, 10 h, 48 min

where $\Delta\theta = \frac{\Delta T}{T_h - T_f}$.

3 Numerical method

To analyze the present problem, the obtained set of Eqs. (14)–(19a, 19b, 19c, 19d) along with the boundary conditions Eqs. (19a, 19b, 19c, 19d) have been calculated using the powerful method that is called the finite element [32, 33]. The continuity equation, Eq. (14), is employed as a constraint to satisfy the mass conservation. Hence, the constraint for continuity equation is introduced as a penalty parameter (χ) in the momentum equations as described by Reddy [33]. Therefore, the pressure is written as:

$$P = -\chi\left(\frac{\partial U}{\partial X} + \frac{\partial V}{\partial Y}\right) \quad (21)$$

Using Eq. (21), the momentum equations are reduced as:

$$\frac{\partial U}{\partial Fo} + U\frac{\partial U}{\partial X} + V\frac{\partial U}{\partial Y} = -\frac{\partial}{\partial X}$$
$$\times \left(\chi\left(\frac{\partial U}{\partial X} + \frac{\partial V}{\partial Y}\right)\right) + \text{Pr}\left(\frac{\partial U}{\partial X} + \frac{\partial U}{\partial Y}\right) + S(\theta)\,U \quad (22)$$

$$\frac{\partial V}{\partial Fo} + U\frac{\partial V}{\partial X} + V\frac{\partial V}{\partial Y} = -\frac{\partial}{\partial Y}\left(\chi\left(\frac{\partial U}{\partial X} + \frac{\partial V}{\partial Y}\right)\right) + \text{Pr}\left(\frac{\partial V}{\partial X} + \frac{\partial V}{\partial Y}\right)$$
$$+ \text{Ra}\,\text{Pr}\,\theta - (\text{Ha})^2\,\text{Pr}\cdot V + S(\theta)\,V \quad (23)$$

Thus, in the above equations the continuity Eq. (8) is satisfied for very large values of the penalty parameter ($\chi = 10^7$) [33]. Now, the velocities (U and V) as well as the temperature are expanded invoking a basis set $\{\zeta_k\}_{k=1}^N$ as,
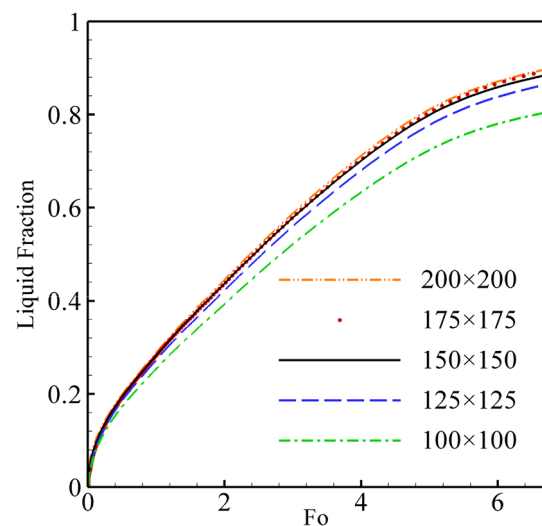

Fig. 2 The melting interface for various grid sizes

$$U \approx \sum_{k=1}^{N} U_k \zeta(X,Y), \quad V \approx \sum_{k=1}^{N} V_k \zeta(X,Y), \quad \theta \approx \sum_{k=1}^{N} \theta_k \zeta(X,Y)$$
(24)

for $-0.5 < X < +0.5$ and $0 < Y < 1$. It should be noted that the basic functions for U and V velocities and the temperature are the same, and thus, the total number of nodes variables is N. Invoking the Galerkin finite element method, the non-linear residual for the governing equations of momentum Eqs. (22) and (23) as well as the energy equation Eq. (17) at nodes of internal domain Ω are derived as,

$$R_i^1 = \sum_{k=1}^{N} U_k \int_{\Omega} \frac{\partial \xi_K}{\partial F_0} dXdY + \sum_{k=1}^{N} U_k \int_{\Omega} \left[\left(\sum_{k=1}^{N} U_k \zeta_k \right) \frac{\partial \zeta_k}{\partial X} \zeta_k dXdY \right.$$
$$\left. + \left(\sum_{k=1}^{N} V_k \zeta_k \right) \frac{\partial \zeta_k}{\partial Y} \zeta_k dXdY \right] \zeta_i dXdY$$
$$+ \sum_{k=1}^{N} U_k \int_{\Omega} \frac{\partial \xi_i}{\partial X} \left[(\chi) \frac{\partial \xi_K}{\partial X} dXdY \right]$$
$$+ \sum_{k=1}^{N} V_k \int_{\Omega} \frac{\partial \xi_i}{\partial X} \left[(\chi) \frac{\partial \xi_K}{\partial Y} dXdY \right]$$
$$+ Pr \sum_{k=1}^{N} U_k \int_{\Omega} \left[\frac{\partial \xi_i}{\partial X} \frac{\partial \xi_K}{\partial X} + \frac{\partial \xi_i}{\partial Y} \frac{\partial \xi_K}{\partial Y} \right] dXdY$$
$$+ S(\theta) \sum_{k=1}^{N} \int_{\Omega} \left(\sum_{k=1}^{N} (U_k \zeta_k) \zeta_i \right) dXdY$$
(25)

$$R_i^2 = \sum_{k=1}^{N} V_k \int_{\Omega} \frac{\partial \xi_K}{\partial F_0} dXdY$$
$$+ \sum_{k=1}^{N} V_k \int_{\Omega} \left[\left(\sum_{k=1}^{N} U_k \zeta_k \right) \frac{\partial \zeta_k}{\partial X} + \left(\sum_{k=1}^{N} V_k \zeta_k \right) \frac{\partial \zeta_k}{\partial Y} \right] \zeta_i dXdY$$
$$+ \sum_{k=1}^{N} U_k \int_{\Omega} \frac{\partial \xi_i}{\partial Y} \left[(\chi) \frac{\partial \xi_K}{\partial X} dXdY \right]$$
$$+ \sum_{k=1}^{N} V_k \int_{\Omega} \frac{\partial \xi_i}{\partial Y} \left[(\chi) \frac{\partial \xi_K}{\partial Y} dXdY \right]$$
$$+ Pr \sum_{k=1}^{N} V_k \int_{\Omega} \left[\frac{\partial \xi_i}{\partial X} \frac{\partial \xi_K}{\partial X} + \frac{\partial \xi_i}{\partial Y} \frac{\partial \xi_K}{\partial Y} \right] dXdY$$
$$+ Ra\, Pr \int_{\Omega} \left(\sum_{k=1}^{N} \theta_k \zeta_k \right) \zeta_i dXdY$$
$$+ (Ha)^2 Pr \sum_{k=1}^{N} \int_{\Omega} \left(\sum_{k=1}^{N} V_k \zeta_k \right) \zeta_i dXdY$$
$$+ S(\theta) \sum_{k=1}^{N} \int_{\Omega} \left(\sum_{k=1}^{N} (V_k \zeta_k) \zeta_i \right) dXdY$$
(26)

$$R_i^3 = \sum_{k=1}^{N} \theta_k \int_{\Omega} \frac{\partial \xi_K}{\partial F_0} \zeta_i dXdY$$
$$+ \sum_{k=1}^{N} \theta_k \int_{\Omega} \left[\left(\sum_{k=1}^{N} U_k \zeta_k \right) \frac{\partial \zeta_k}{\partial X} + \left(\sum_{k=1}^{N} V_k \zeta_k \right) \frac{\partial \zeta_k}{\partial Y} \right] \zeta_i dXdY$$
$$+ \gamma \sum_{k=1}^{N} \theta_k \int_{\Omega} \left[\frac{\partial \xi_i}{\partial X} \frac{\partial \xi_K}{\partial X} + \frac{\partial \xi_i}{\partial Y} \frac{\partial \xi_K}{\partial Y} \right] dXdY$$
$$+ \frac{1}{Ste} \sum_{k=1}^{N} \varphi_k(\theta) \int_{\Omega} \frac{\partial \xi_K}{\partial F_0} \zeta_i dXdY,$$
(27)

where the linear basis functions are adopted. The three-point Gaussian quadrature is also utilized to evaluate the integrals terms in the Eqs. (25)–(26). Considering the momentum equations, the terms incorporating the penalty parameter (χ) are computed using the two-point Gaussian quadrature employing the reduced integration penalty formulation [33]. The non-linear residual equations, Eqs. (25)–(27), are solved by the Newton–Raphson method to compute the coefficients of the expansions (i.e. U_k, V_k and θ_k) in Eq. (24). The detailed solution procedure could be found in [32, 34]. Additionally, uniform meshes in both the X and Y directions are adopted in which the discretized equations are implemented. Therefore, the utilized elements are quadrilateral elements. Considering the quadrilateral elements, ζ can be linearly approximated as $c_1 + c_2 X + c_3 Y + c_4 XY$ where c_1–c_4 are coefficients which can be obtained using the grid points. For each of the initial velocity and initial temperature, a value of zero is selected as initial guesses. The iteration process commenced until the residuals for the momentum residual equation, i.e. $j = 1$ and 2, and the heat equation, i.e. $j = 3$, satisfy $\sum (R_i^j) \leq 10^{-7}$. A backward differentiation formula (BDF) of variable order (between 1 and 2) associated with free time steps is utilized [35]. The results of the present code have been successfully validated against the numerical and experimental results of phase-change heat transfer in a cavity filled with phase-change materials [21, 23] and against the works conducted by Sathiyamoorthy and Chamkha [6, 7] who have examined the natural convection flow under a magnetic field in a square cavity filled with an electrically-conducting fluid.

3.1 Grid check

In order to check the grid independency of the solution, the calculations were repeated for several grid sizes in the case of $A_{mush} = 1 \times 10^5$, $\Delta T = 0.05$ K, $Pr = 0.0216$,
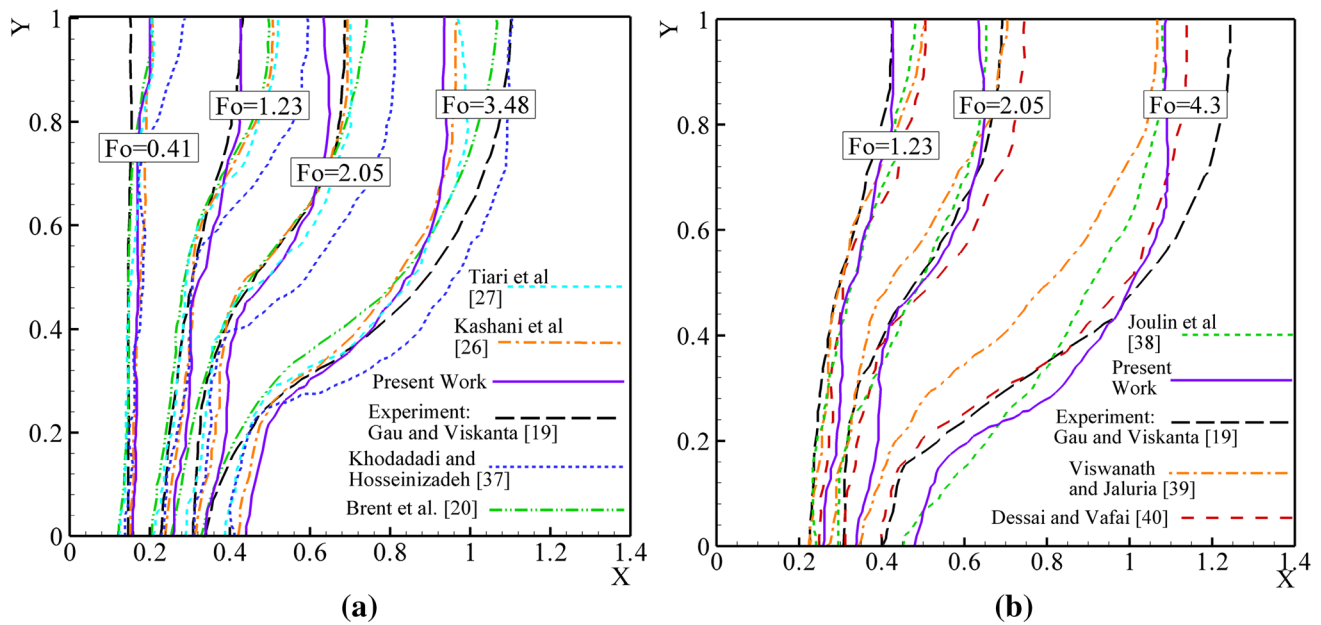
Fig. 3 A comparison between the experimental and numerical results available in literature and the present results when $\gamma = 1$ and neglecting the magnetic effects **a**, **b** uniformly heated left and cooled right and the bottom and top walls are insulated, Ra = 6×10^5 Pr = 0.0216

Ra = 1×10^5, Ste = 0.039, $\gamma = 1$. Table 1 indicates the required time for simulation of about 90% of melting for various grid sizes. The liquid fraction for different grid sizes is also depicted in Fig. 2. The results of Fig. 2 indicate that the grid size of 150 × 150 can provide acceptable accuracy. Hence, the results of the present study are carried out using the grid size 150 × 150.

3.2 Validation of the results

To check the precision of the solution, several investigations have been performed. As the first case, the experimental results of Gau and Viskanta [19] and the numerical results available in literature for a rectangular cavity with aspect ratio (height/width) of 0.714 are adopted and compared with the results of the current study. In the experiment of Gau and Viskanta [19], the left wall is hot while the top and bottom walls are insulated.

Gau and Viskanta [19] have evaluated the melting interface using the pour-out method and the probing method. The evaluated melting interface for this problem is also numerically addressed by Kashani et al. [26], Tiari et al. [27], Khodadadi and Hosseinizadeh [36], Berant et al. [20], Joulin et al. [37], Viswanta and Jaluria [38] and Desai and Vafai [39]. The summary of the available numerical results are plotted in Fig. 3a, b. As seen, the results of the present study are in reasonable agreement with the available experimental and numerical results. In the case of $F_0 = 3.48$, the results are somehow different from the experiment but in
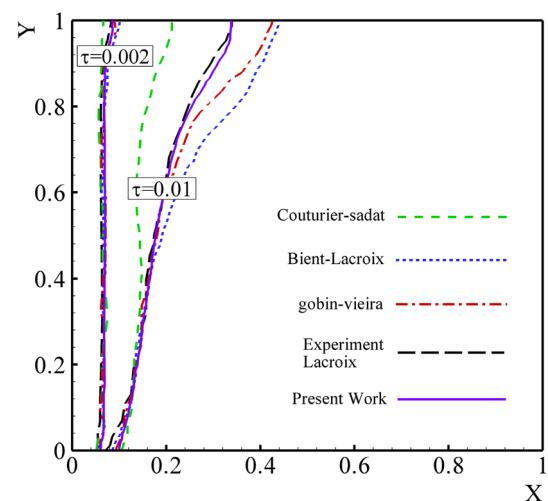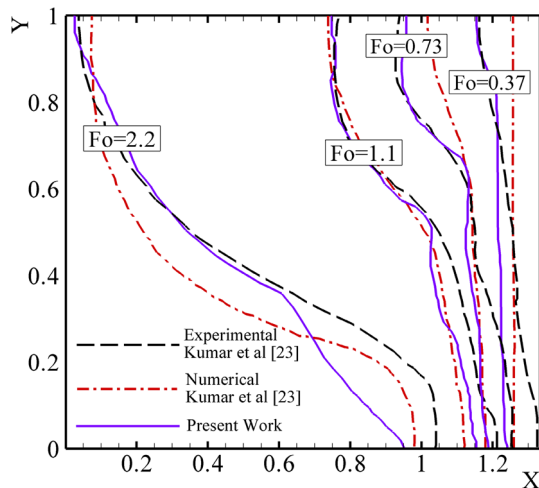

Fig. 4 A comparison between the melting interface reported by Bertrand et al. [21] and the current results ($\tau = F_0 \times$ Ste)

agreement with the numerical results. The previous authors have concluded that the difference between the numerical and experimental results in this case could be due to the method of evaluating the melting interface in the experiment of Gau and Viskanta [19]. The authors have measured the melting interface mechanically using a manual mechanical probe. For high values of F_0 the solid–liquid interface of melting could be unstable, and hence, distinguishing the precise shape of interface is hard.

As another validation, the benchmark study of Bertrand et al. [21] is adopted in a case in which Ra = 1×10^7,

Table 2 Input provided for one case in simulation Kumar et al. [23]

Heater input (right side)	Stefan number	Prandtl number	Rayleigh number	Hartmann number	Temp at left side (K)	Temp at right side (K)
16.3 kW/m^2	0.4	0.0236	1.4×10^7	0	555	599

Fig. 5 A comparison between the results of benchmark study of Kumar et al. [23] and the current results at different non-dimensional time steps of $F_0 = 0.37$, $F_0 = 0.73$, $F_0 = 1.10$ and $F_0 = 2.2$

Pr = 50, Ha = 0 and $\gamma = 1$. A literature review shows that many researchers have compared their numerical results with the benchmark results reported by Bertrand et al. [21]. Figure 4 shows the melting interface evaluated in the previous studies and those reported by Bertrand et al. [21]. The results of the current study have also been plotted in Fig. 4 as a comparison. This figure shows that the present numerical results are in very close agreement with the experimental results.

Also, as another comparison, the results of the present study are compared with the experimental results reported by Kumar et al. [23] for melting of lead. Kumar et al. [23] have examined the melting of lead contained in a stainless steel cuboid. In the study of Kumar et al. [23], there was a heater mounted at one of the vertical side walls of the cavity which provided a constant heat flux, while the other walls were insulated. The authors have carried out the photography of solid–liquid interface movement during melting of lead using neutron radiography. The non-dimensional parameters of the experiment set-up of Kumar et al. [23] are shown in Table 2. Initially, heater is put on and temperature will increase on both sides. In the experiment of Kumar et al. [23], when melting commenced, the temperature at the right hand side wall (the heater side) was higher than that of the left hand side wall. Therefore, a linear temperature distribution was the initial condition for the commencing of the melting process. As Kumar et al. [23]

have performed the experiment for the case of constant heat flux, the Rayleigh number and Stefan number are needed to be calculated on the basis of the constant heat flux as: Ste* = $C_p q''_{cond} L_x/(kL)$ and Rayleigh number based on constant heat flux is given by Ra* = $g\beta q''_{cond} L_y^4/(k\alpha\nu)$.

Here, the results of the present study are compared with the experimental results reported by Kumar et al. [23] (Fig. 5).

As seen, the results of the present study are in very good agreement with the experimental results reported by Kumar et al. [23].

For the case of magnetohydrodynamic flows, Sathiyamoorthy and Chamkha [7] have studied the effect of the presence of magnetic effects on natural convection of electrically-conducting liquids. The top and left walls of the cavity in the study of Sathiyamoorthy and Chamkha [7] are considered to be isothermal at the hot temperature of T_h. The top and right walls are also considered to be isothermal at the cold temperature of T_c. Here, As a comparison, the current results are compared with the results of Sathiyamoorthy and Chamkha [7] by assuming that the cavity is filled with a molten metal and the same boundary conditions as described in [7]. Figure 6 shows a comparison between the streamlines and isotherms reported by Sathiyamoorthy and Chamkha [7] and the results of the current study when Ra = 10^5, Pr = 0.054 and two Hartmann numbers of $Ha = 50$ and Ha = 100. Figure 6 indicates good agreement between the both studies.

As yet another comparison for the magnetic field effect, the results of the current research are compared with the finding of Al-Mudhaf and Chamkha [40]. Al-Mudhaf and Chamkha [40] have studied numerically the natural convective flow of electrically-conducting gallium and germanium liquid metals in an inclined rectangular enclosure in the presence of a uniform magnetic field due to a transverse temperature gradient. The results of the comparison between these two studies have been summarized in Table 3 when Ra = 10^5, Pr = 0.025, S = 45° (where S is the enclosure inclination angle).

4 Results and discussion

Now, as a case study, consider a cavity with the size of $L_x = 6.35$ cm, $L_y = 6.35$ cm filled with gallium. The temperature at the hot wall is $T_h = 38$ °C and at the cold wall is $T_c = 28.3$ °C. The thermophysical properties of gallium

Fig. 6 Isotherms and streamlines with reference to Sathiyamoorthy and Chamkha [7] and the results of present study

Streamlines | Isotherms
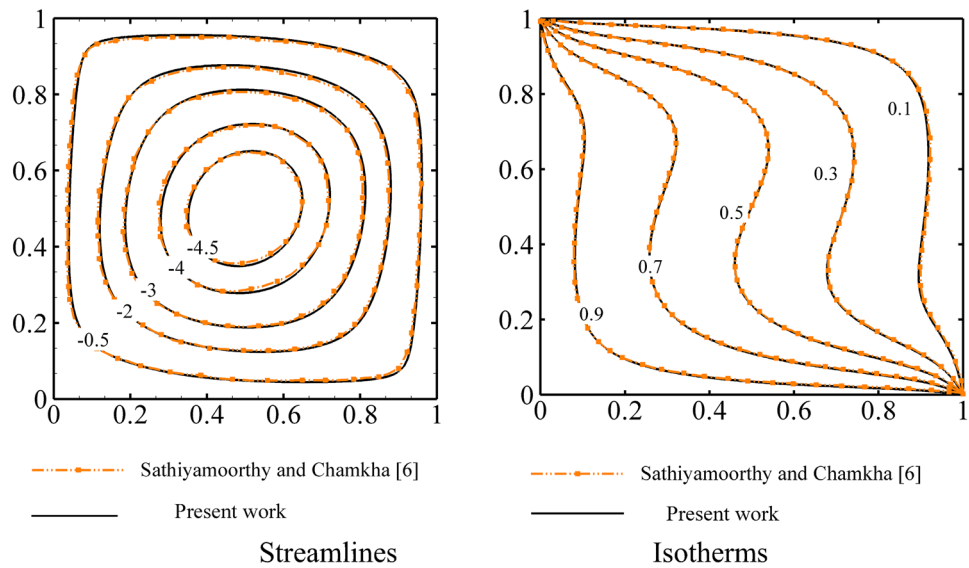
(a) Ha=50
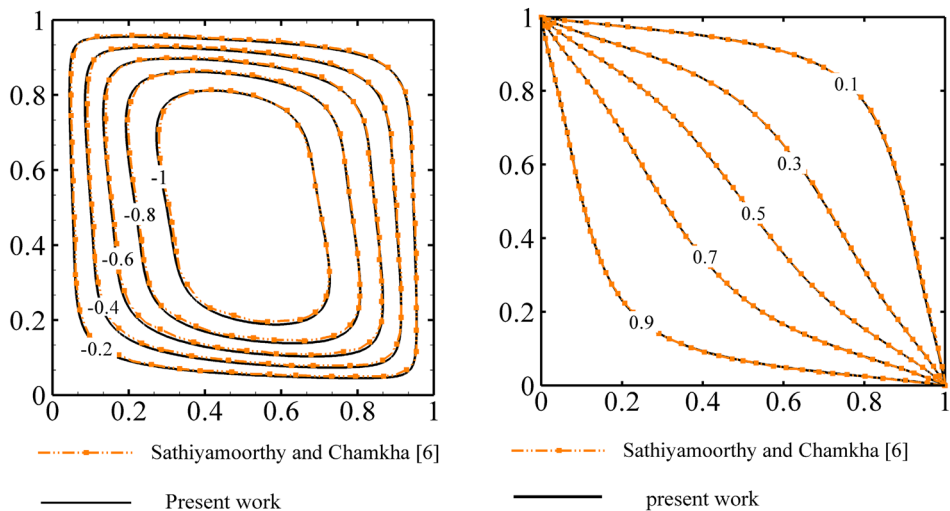
(b) Ha=100

Table 3 The average Nusselt number, $\overline{Nu}$ reported by Al-Mudhaf and Chamkha [40] and the present research

Ha	Al-Mudhaf and Chamkha [40]	Present study
30	2.78	2.67
50	1.86	1.81
70	1.43	1.39
100	1.14	1.12

are represented in Table 4. In this case, the corresponding non-dimensional parameters are: Pr = 0.0216, Ste = 0.039, Ra = 6×10^5 and $\gamma = 1$. These non-dimensional parameters

Table 4 Thermophysical of pure gallium

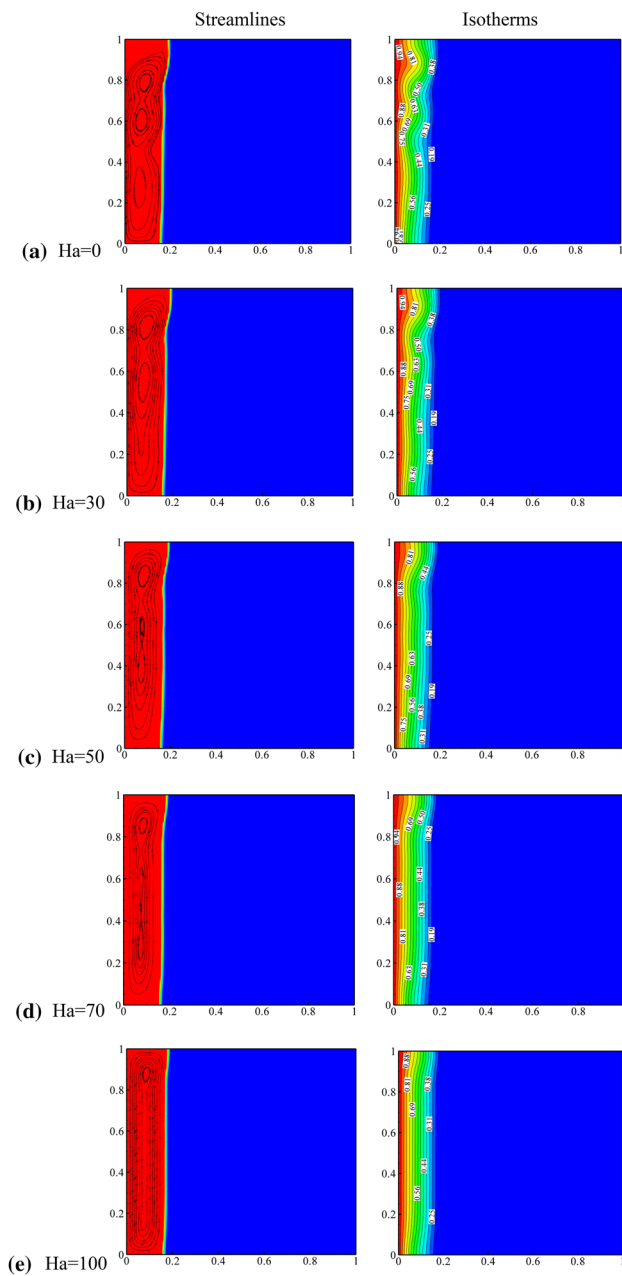| Property	Symbol	Value	Unit
Density (solid/liquid)	ρ	6093	(kg/m^3)
Thermal expansion coefficient	β	1.2×10^{-4}	(1/K)
Fusion temperature	T_f	302.85	K
Thermal conductivity (solid/liquid)	k	32.0	(W/m K)
Latent heat of fusion	L	80,160	(J/kg)
Specific heat capacity (solid/liquid)	C	381.5	(J/kg K)
Dynamic viscosity	μ	1.81×10^{-3}	(kg/m .s)

Fig. 7 Isotherms and streamlines for $\tau = F_0 \times$ Ste $= 0.015$ when **a** Ha $= 0$, **b** Ha $= 30$, **c** Ha $= 50$, **d** Ha $= 70$, **e** Ha $= 100$

Fig. 8 The melting interface for various Hartmann numbers at $\tau = 0.015$

are considered as the default non-dimensional parameters in this study and the calculations are performed for these set of non-dimensional parameters otherwise they will be stated.

Figure 7 shows the streamlines and isotherms of the melting process at the beginning of the melting process, i.e. $\tau = F_0 \times$ Ste $= 0.015$, for various values of the magnetic field strength when Ra $= 6 \times 10^5$. At the background of the streamlines figures, the contours of the volume fraction of the liquid phase (φ) are plotted. As seen, the liquid phase is commenced in the vicinity of the hot wall. A large region

near the cold wall is remained frozen yet. A fast variation of the volume fraction from unity (only liquid) to zero (only solid) occurs at the interface, controlled by Eq. (21) as a function of temperature. These figures demonstrate that the increase of the Hartmann number slightly affects the melting process. It is clear that the magnetic field effect tends to reduce the velocity of the fluid as it is always against the motion of the fluid. At the beginning of the melting process, there is a narrow region filled with molten trapped between two solid walls (the heater and the melting interface). Therefore, the fluid motion is slow, and the variation of the magnetic field could not induce a significant effect on the motion and melting process. Figure 8 depicts the shape of the interface at the non-dimensional time step of $\tau = 0.015$ for various values of the Hartmann number. This figure is in agreement with the results of Fig. 7 and indicates that the presence of the magnetic field is not important at the beginning stages of the melting process.

Figure 9 shows the streamlines and isotherms of the melting process at time step of $\tau = 0.04$ for various values of Ha. This figure indicates that after elapsing of a while, the melting interface is pushed forward into the frozen area. When the magnetic field is weak (i.e. Fig. 9a, b), there are three circulation cells in the molten region. These circulation flows take the heat from the hot wall and try to distribute it on the frozen interface. Hence, regarding the three circulation flow streams, three caved regions on the interface can be seen. As the magnetic field gets strong, the circulation cells break down into a large circulation cell. In this case, the caved regions disappeared and obviously the molten rate is decreased. A comparison between the shapes of the solid–liquid interfaces is depicted in Fig. 10. This figure demonstrates that the increase of the Hartmann number
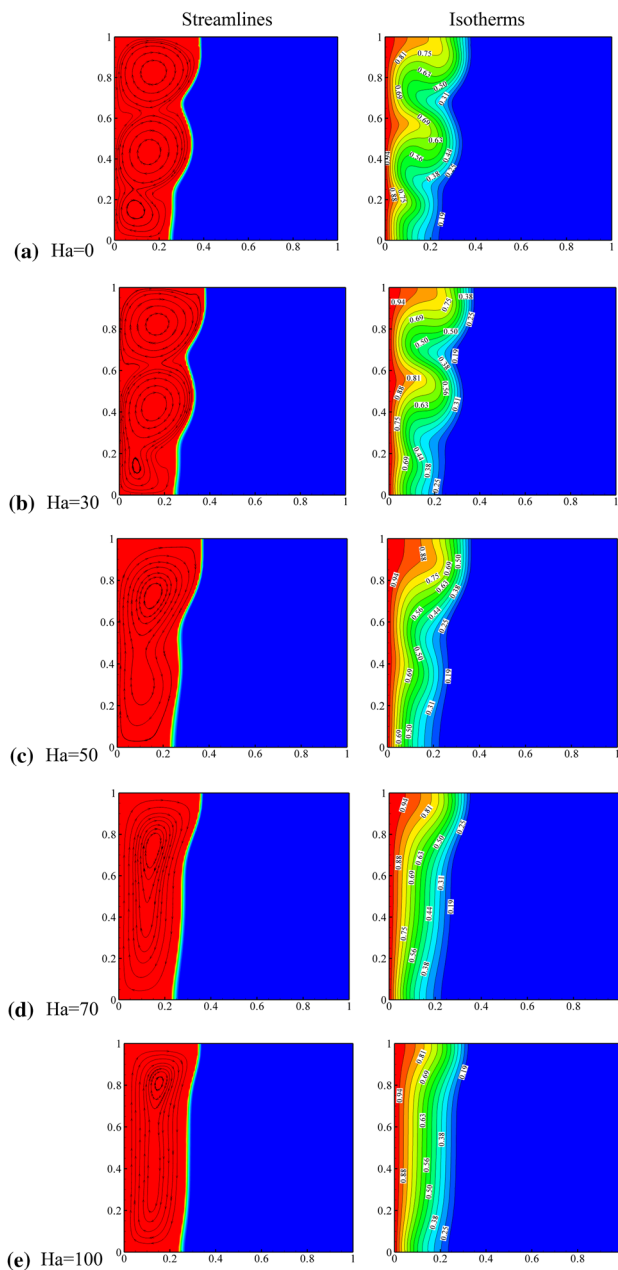
Fig. 9 Isotherms and streamlines for $\tau = F_0 \times$ Ste $= 0.04$ when **a** Ha $= 0$, **b** Ha $= 30$, **c** Ha $= 50$, **d** Ha $= 70$, **e** Ha $= 100$
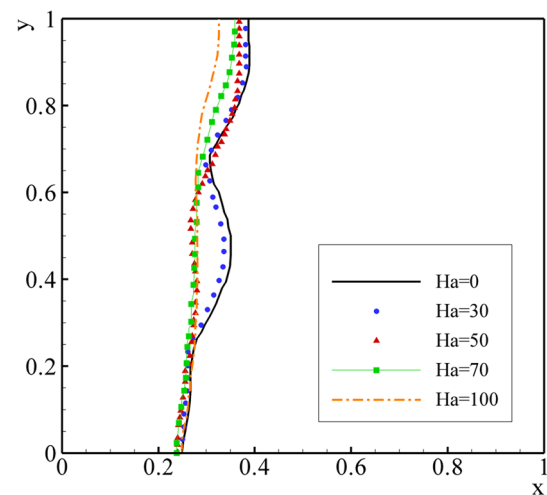

Fig. 10 The melting interface for various Hartmann numbers at $\tau = 0.04$

presence of a weak magnetic field reduces the circulation patterns into just two. The further increase of the magnetic field effect results in large circulation patterns and prevents the formation of local circulation patterns.

This figure indicates that the effect of the magnetic field is more obvious in the top side of the cavity rather than the bottom side. Indeed, the molten liquid absorbs the heat by conduction from the hot plate, and then it moves upward due to the buoyancy forces. Therefore, the top of cavity in the molten region is filled with a hot molten. Then, the hot molten interacts with the cold interface and moves downward. As a result, there is a large caved area filled with molten near the top of the cavity. As the hot molten at the top moves downward and interacts with the cold frozen interface, it loses heat and gets colder and colder. Therefore, when the molten reaches the bottom of the cavity, it has lost a considerable amount of heat, and hence, the molten region at the bottom of the cavity is a narrow area. Figure 12 summarizes the obtained solid–liquid interface at the non-dimensional time of $\tau = 0.08$ for various values of the magnetic field parameter (Ha). As seen in Fig. 12, the position of the interface at the bottom of the cavity is not a monotonic function of Ha. As the Hartmann number increases, the interface moves towards the hot plate, until the Hartmann number is around Ha $= 70$ and then it moves back toward the cold wall.

As mentioned, at the bottom part of the cavity, the change in the position of the interface is not a monotonic function of the magnetic field strength (Ha). Indeed, the position and the shape of the interface are functions of the convective and diffusive heat transfer mechanisms. When the Hartmann number is small, the increase of Ha mostly affects the fluid velocity at the regions where the fluid velocity is high. In this region, which is about the
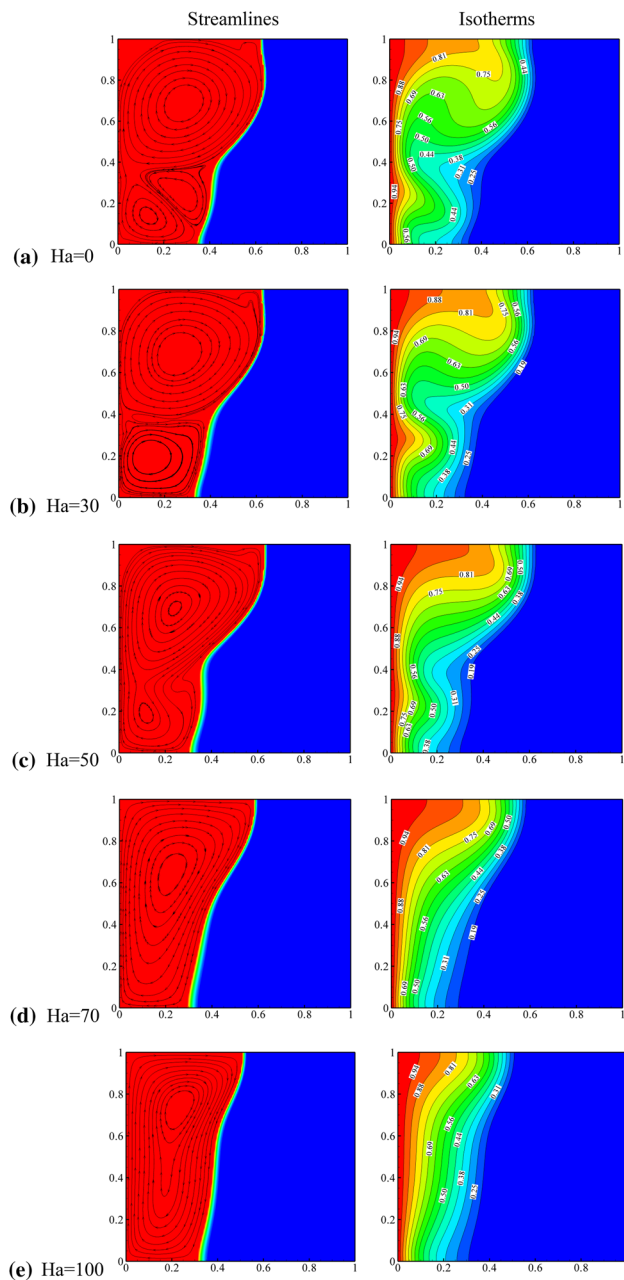
results in a smoother interface shape, but it decreases the molten volume fraction.

Figure 11 demonstrates the effect of the Hartmann number on the streamlines and isotherms in the cavity at the non-dimensional time of $\tau = 0.08$. This time for the melting of gallium as described at the beginning of this section is equivalent to 10 min from the beginning of the melting process. Figure 11a is in agreement with Fig. 9a and confirms the presence of three circular flows in the absence of the magnetic field effect. Figure 11b depicts that the

Fig. 11 Isotherms and streamlines for $\tau = F_0 \times Ste = 0.08$ when **a** Ha = 0, **b** Ha = 30, **c** Ha = 50, **d** Ha = 70, **e** Ha = 100

Fig. 12 The melting interface for various Hartmann numbers at $\tau = 0.08$

middle height of the cavity next to the melting interface, the shape of the mushy region and the melting interface is under the significant influence of the variation of the magnetic field. Consequently, the shape of the interface at the upper regions of the cavity gives directions to the fluid flow moving from the upper to the lower side along the melting interface. Hence, the shape of the interface near the bottom of the cavity is under the influence of the fluid flow. As a result, and as seen for the low values of the Hartmann
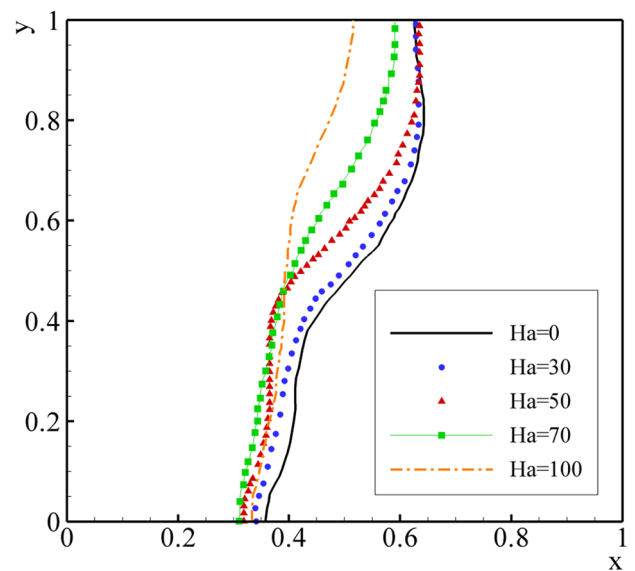
number, (Ha = 0–50), the position of the melting interface next to the bottom part of the cavity almost follows the expected flow patterns monastically. However, as the Hartmann number gets very strong, it almost suppresses the natural convection flows and significantly decreases the melting volume fraction. In this case, the overall position of the melting interface is seized to advance and the interface shape also gets flattened. Therefore, in this case, a different trend of behavior for the change in the location of the melting interface at the bottom part of the cavity can be seen. As a summary, it can be said that the shape and the position of the melting interface at the bottom part of the cavity are functions of the shape of the interface at the upper region of the cavity as well as the overall position of the melting interface. The change in the Hartmann number has the tendency to change the shape of the interface at the upper region as well as the overall position of the melting interface (the melting volume fraction), and hence, based on the magnitude of the Hartmann number, two different trends of change in the position of the melting interface at the bottom part of the cavity can be expected.

Figure 13 illustrates the streamlines and isotherms contours inside the cavity in the non-dimensional time of $\tau = 0.15$ for various values of the Hartmann number. In this case, most regions of the cavity are filled with the liquid phase and the fluid can freely move inside the cavity. A jet of hot fluid is present near the hot wall which drives the hot liquid upward. There is also a downward jet of cold liquid at the interface side. The hot liquid is almost present along the top wall while the cold liquid exists along the bottom
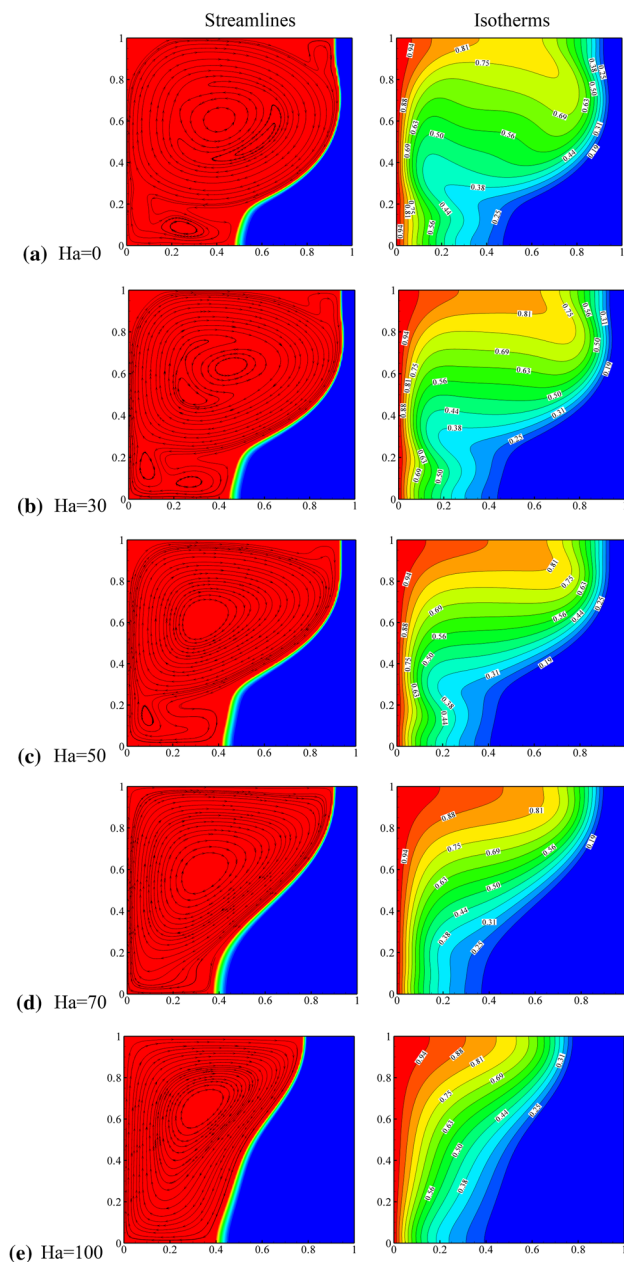
Fig. 13 Isotherms and streamlines for $\tau = F_0 \times Ste = 0.15$ when **a** Ha = 0, **b** Ha = 30, **c** Ha = 50, **d** Ha = 70, **e** Ha = 100

Fig. 14 The melting interface for various Hartmann numbers at $\tau = 0.15$

wall. There is a stratified region at the core of the cavity in which the heat transfer occurs in the vertical direction from top to bottom. Near the bottom of the cavity, there is a local slow circulation regime which results in a very low temperature gradient at the bottom of the cavity near the solid–liquid interface region (the mushy region). At this region where the temperature gradient is low and almost linear, the thickness of the mushy region is also increased (as seen in the volume fraction contours in the background of the streamline contours). Figure 14 surmises the melting

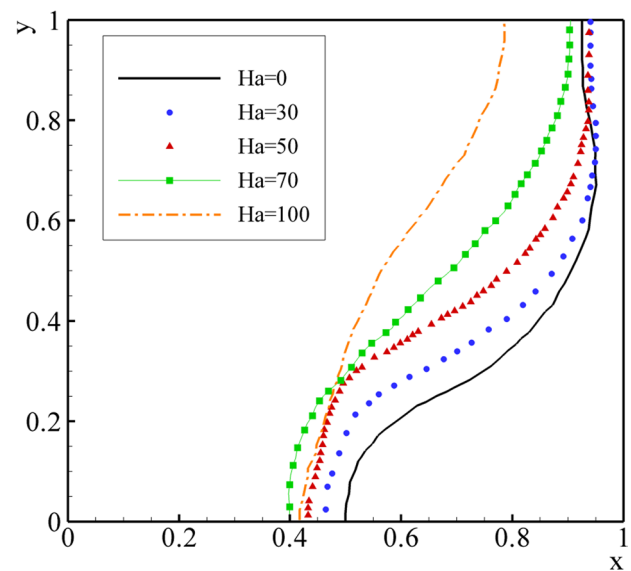interfaces for various values of the Hartmann number when $\tau = 0.15$. This figure shows that the trend of the motion of the interface at the bottom of the cavity follows the trend of behavior observed in Fig. 12. For low values of the Hartmann number, e.g. Ha = 30 and 50, the melting interface is closer to the cold wall compared to that of Ha = 0. In contrast, the melting interface for high values of the Hartmann number, e.g. Ha = 70 and 100, is not as close to the cold wall as that of Ha = 0. This is because of the fact that the presence of the magnetic field induces a magnetic force that tends to suppress the natural convection velocity in the cavity. The decrease of velocity reduces the strength of the advective heat transfer mechanism in the cavity. Thus, the more increase of the magnetic field (the raise of Ha) the more the suppression of melting.

It is also interesting that for the cases of Ha = 0, 30 and 50, the temperature gradients next to the hot wall and the melting front (melting interface) are strong and the isotherms are close together. The temperature distribution in the core of the cavity is almost horizontal. This trend of behavior is similar to the temperature distribution for a regular cavity with a high Rayleigh number [41]. However, as the Hartmann number increases (Ha = 70 and 100), the gradients of temperature next to the hot wall and the melting front decrease and the temperature distribution forms almost a vertical shape. This temperature distribution could be of interest in some of the engineering applications or in a metallurgical process where a uniform temperature distribution is demanded.

Figure 15 shows the overall volume fraction of the molten phase, i.e. the liquid phase, as a function of the
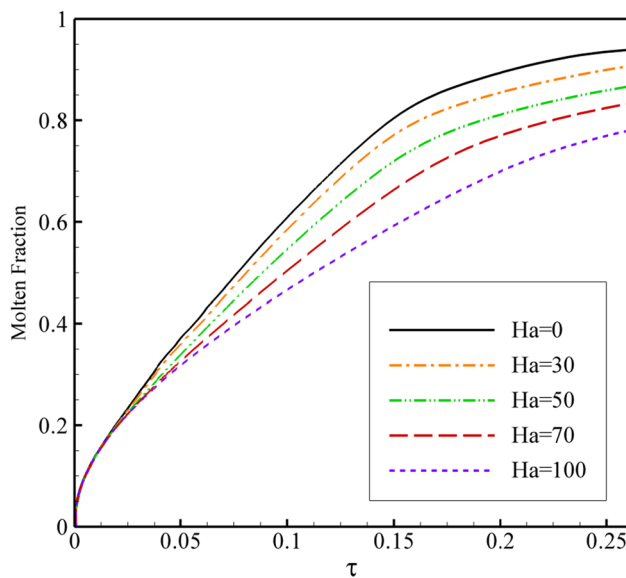
Fig. 15 Effect of magnetic induction on liquid fraction for various Hartmann numbers

non-dimensional time (τ) for Hartmann numbers in the range Ha = 0–100. As observed in Fig. 9, at the early stages of the melting process, the conduction heat transfer is the dominant effect in the cavity, and hence, the effect of the presence of the magnetic field is negligible. As the fraction of the liquid phase increases and the molten region gets wider, the natural convective flows get stronger, which boosts the effect of the magnetic field. As mentioned, the magnetic field tends to decrease the velocity of the molten as it always acts against the motion direction of the fluid. The decrease of the molten motion results in the decrease of the convective heat transfer in the cavity. As the Hartmann number increases, the effect of the magnetic field increases. Therefore, as seen in Fig. 15, the increase of Ha results in decreases in the molten volume fraction.

5 Conclusion

The impact of magnetic induction on the melting process of a metallic electrically-conducting phase-change material (PCM) in an enclosure was investigated. There was a temperature difference between the side walls of the cavity and the bottom and top walls were well insulated. An enthalpy-porosity approach was utilized to model the phase-change process. The effect of buoyancy forces were taken into account using the Boussinesq model. The results of the present study were compared with different numerical and experimental results available in the literature and were found in good agreement. The results were reported in the form of the melting volume fraction and contours to

study the effect of the magnetic field (Hartmann number) on phase-change heat transfer and melting behavior of an electrically-conducting PCM in the cavity. The results showed that the increase of the Hartmann number would decrease the rate of phase-change process. The presence of a uniform magnetic field was found to play an effective role in the melting front and controlled velocity of flow. Of course, it is important to notice that even in the case of a strong applied magnetic field, i.e. Ha = 100, the melt front area in the upper parts of the enclosure was still in a convex shape, and hence, the melting front was not perfectly uniform.

Since in the present study, the angle of the magnetic field was assumed to be constant in the horizontal direction, the magnetic controlling parameter was solely the Hartmann number. The results demonstrated that the increase of the intensity of the applied magnetic field (increase of Hartmann number) could suppress the flow velocity, but it could not well control the temperature distribution and the melting front shape. However, the change in the inclination angle of the magnetic field may induce more significant controlling mechanism on the flow, heat transfer and the melting front which can be studied in future researches.

References

1. Stefanescu D (2015) Science and engineering of casting solidification. Springer, London
2. Tournier RF, Beaugnon E (2009) Texturing by cooling a metallic melt in a magnetic field. Sci Technol Adv Mater 10:014501
3. Sheikholeslami M, Bandpy MG, Ellahi R, Zeeshan A (2014) Simulation of MHD CuO–water nanofluid flow and convective heat transfer considering Lorentz forces. J Magn Magn Mater 369:69–80
4. Kabeel A, El-Said EM, Dafea S (2015) A review of magnetic field effects on flow and heat transfer in liquids: present status and future potential for studies and applications. Renew Sustain Energy Rev 45:830–837
5. Borges EM, Braz Filho FA, Guimaraes LNF (2006) Liquid metal flow control by DC electromagnetic pumps. In: Proceedings of the 11th Brazilian congress of thermal sciences and engineering, Curitiba, Brazil, Dec 5–8
6. Sathiyamoorthy M, Chamkha A (2010) Effect of magnetic field on natural convection flow in a liquid gallium filled square cavity for linearly heated side wall(s). Int J Therm Sci 49(9):1856–1865
7. Sathiyamoorthy M, Chamkha AJ (2012) Natural convection flow under magnetic field in a square cavity for uniformly (or) linearly heated adjacent walls. Int J Numer Meth Heat Fluid Flow 22(5):677–698
8. Gontijo R, Cunha F (2012) Experimental investigation on thermo-magnetic convection inside cavities. J Nanosci Nanotechnol 12(12):9198–9207

9. Maatki C, Kolsi L, Oztop HF, Chamkha A, Borjini MN, Aissia HB, Al-Salem K (2013) Effects of magnetic field on 3D double diffusive convection in a cubic cavity filled with a binary mixture. Int Commun Heat Mass Transf 49:86–95

10. Selimefendigil F, Öztop HF, Al-Salem K (2014) Natural convection of ferrofluids in partially heated square enclosures. J Magn Magn Mater 372:122–133

11. Sheikholeslami M, Bandpy MG, Ellahi R, Hassan M, Soleimani S (2014) Effects of MHD on Cu–water nanofluid flow and heat transfer by means of CVFEM. J Magn Magn Mater 349:188–200

12. Jena SK, Yettella VKR, Sandeep CPR, Mahapatra SK, Chamkha AJ (2014) Three-dimensional Rayleigh–Bénard convection of molten gallium in a rotating cuboid under the influence of a vertical magnetic field. Int J Heat Mass Transf 78:341–353

13. Malvandi A, Safaei M, Kaffash M, Ganji D (2015) MHD mixed convection in a vertical annulus filled with Al_2O_3–water nanofluid considering nanoparticle migration. J Magn Magn Mater 382:296–306

14. Adesanya S, Oluwadare E, Falade J, Makinde O (2015) Hydromagnetic natural convection flow between vertical parallel plates with time-periodic boundary conditions. J Magn Magn Mater 396:295–303

15. Chamkha A, Ismael M, Kasaeipoor A, Armaghani T (2016) Entropy generation and natural convection of CuO–Water nanofluid in C-shaped cavity under magnetic field. Entropy 18(2):50

16. Mojumder S, Rabbi KM, Saha S, Hasan M, Saha SC (2016) Magnetic field effect on natural convection and entropy generation in a half-moon shaped cavity with semi-circular bottom heater having different ferrofluid inside. J Magn Magn Mater 407:412–424

17. Selimefendigil F, Öztop HF, Chamkha AJ (2016) MHD mixed convection and entropy generation of nanofluid filled lid driven cavity under the influence of inclined magnetic fields imposed to its upper and lower diagonal triangular domains. J Magn Magn Mater 406:266–281

18. Rashidi M, Nasiri M, Khezerloo M, Laraqi N (2016) Numerical investigation of magnetic field effect on mixed convection heat transfer of nanofluid in a channel with sinusoidal walls. J Magn Magn Mater 401:159–168

19. Gau C, Viskanta R (1986) Melting and solidification of a pure metal on a vertical wall. J Heat Transf 108(1):174–181

20. Brent A, Voller V, Reid KTJ (1988) Enthalpy-porosity technique for modeling convection-diffusion phase change: application to the melting of a pure metal. Numer Heat Transf Part A Appl 13(3):297–318

21. Bertrand O, Binet B, Combeau H, Couturier S, Delannoy Y, Gobin D, Lacroix M, Le Quéré P, Médale M, Mencinger J (1999) Melting driven by natural convection A comparison exercise: first results. Int J Therm Sci 38(1):5–26

22. Fan L, Khodadadi J (2011) Thermal conductivity enhancement of phase change materials for thermal energy storage: a review. Renew Sustain Energy Rev 15(1):24–46

23. Kumar L, Manjunath B, Patel R, Markandeya S, Agrawal R, Agrawal A, Kashyap Y, Sarkar P, Sinha A, Iyer K (2012) Experimental investigations on melting of lead in a cuboid with constant heat flux boundary condition using thermal neutron radiography. Int J Therm Sci 61:15–27

24. Kumar L, Manjunath B, Patel R, Prabhu S (2014) Experimental investigations on melting of lead in a cuboid with constant heat flux boundary condition at two vertical walls using infra-red thermography. Int J Heat Mass Transf 68:132–140

25. Ranjbar AA, Kashani S, Hosseinizadeh SF, Ghanbarpour M (2011) Numerical heat transfer studies of a latent heat storage system containing nano-enhanced phase change material. Therm Sci 15(1):169–181

26. Kashani S, Ranjbar A, Abdollahzadeh M, Sebti S (2012) Solidification of nano-enhanced phase change material (NEPCM) in a wavy cavity. Heat Mass Transf 48(7):1155–1166

27. Tiari S, Qiu S, Mahdavi M (2015) Numerical study of finned heat pipe-assisted thermal energy storage system with high temperature phase change material. Energy Convers Manag 89:833–842

28. Tiari S, Qiu S, Mahdavi M (2016) Discharging process of a finned heat pipe–assisted thermal energy storage system with high temperature phase change material. Energy Convers Manag 118:426–437

29. Sreenivasan B, Davidson PA, Etay J (2005) On the control of surface waves by a vertical magnetic field. Phys Fluids (1994–Present) 17(11):117101

30. Alpak FO, Lake LW, Embid SM (1999) Validation of a modified Carman–Kozeny equation to model two-phase relative permeabilities. In: SPE annual technical conference and exhibition, Society of Petroleum Engineers

31. Happel J (1958) Viscous flow in multiparticle systems: slow motion of fluids relative to beds of spherical particles. AIChE J 4(2):197–201

32. Basak T, Roy S, Paul T, Pop I (2006) Natural convection in a square cavity filled with a porous medium: effects of various thermal boundary conditions. Int J Heat Mass Transf 49(7):1430–1441

33. Reddy JN (1993) An introduction to the finite element method. McGraw-Hill, New York

34. Basak T, Roy S, Balakrishnan A (2006) Effects of thermal boundary conditions on natural convection flows within a square cavity. Int J Heat Mass Transf 49(23):4525–4535

35. Süli E, Mayers DF (2003) An introduction to numerical analysis. Cambridge University Press, Cambridge

36. Khodadadi J, Hosseinizadeh S (2007) Nanoparticle-enhanced phase change materials (NEPCM) with great potential for improved thermal energy storage. Int Commun Heat Mass Transf 34(5):534–543

37. Joulin A, Younsi Z, Zalewski L, Rousse DR, Lassue S (2009) A numerical study of the melting of phase change material heated from a vertical wall of a rectangular enclosure. Int J Comput Fluid Dyn 23(7):553–566

38. Viswanath R, Jaluria Y (1993) A comparison of different solution methodologies for melting and solidification problems in enclosures. Numer Heat Transf Part B Fundam 24(1):77–105

39. Desai C, Vafai K (1993) A unified examination of the melting process within a two-dimensional rectangular cavity. J Heat Transf 115(4):1072–1075

40. Al-Mudhaf A, Chamkha AJ (2004) Natural convection of liquid metals in an inclined enclosure in the presence of a magnetic field. Int J Fluid Mech Res 31(3):221–243

41. Bejan A (2013) Convection heat transfer. Wiley, New York